Imaging embryonic development with ultrashort pulse microscopy

Holly C. Gibbs
Yuqiang Bai
Arne C. Lekven
Alvin T. Yeh

Imaging embryonic development with ultrashort pulse microscopy

Holly C. Gibbs
Yuqiang Bai
Texas A&M University
Department of Biomedical Engineering
College Station, Texas 77843-3120
E-mail: holly.gibbs.bme@gmail.com

Arne C. Lekven
Texas A&M University
Department of Biology
College Station, Texas 77843-3258

Alvin T. Yeh
Texas A&M University
Department of Biomedical Engineering
College Station, Texas 77843-3120

Abstract. We report the application of ultrashort pulse microscopy (UPM) for integrated imaging of embryonic development at the tissue, cell, and molecular length scales. The UPM is a multimodal imaging platform that utilizes the broad-power spectrum and high-peak power of 10-fs pulses to render two-photon excited signals and the short coherence gate of such pulses to render optical coherence signals. We show that ultrashort pulses efficiently excite cellular autofluorescence in developing zebrafish embryos such that tissues are readily visualized and individual cells can be monitored, providing a potential method for label-free cell tracking. We also show the ability of ultrashort pulses, without tuning, to excite a broad spectrum of fluorescent protein variants for tracking genetically labeled cell lineages in live embryos, with no apparent damage to the embryos. Molecular information at the mRNA transcript level can also be obtained from embryos that have been stained to reveal the localization of the expression of a gene using NBT/BCIP, which we show can be detected with three-dimensional resolution using a combination of two-photon and optical coherence signals. From this demonstration, we conclude that UPM is an efficient and a powerful tool for elucidating the dynamic multiparameter and multiscale mechanisms of embryonic development. © *The Authors. Published by SPIE under a Creative Commons Attribution 3.0 Unported License. Distribution or reproduction of this work in whole or in part requires full attribution of the original publication, including its DOI.* [DOI: 10.1117/1.OE.53.5.051506]

1 Introduction

Embryonic development is the shaping of a single cell into a functioning organism through the interdependent forces of cell proliferation, migration, and genetic specification. Our understanding of embryonic development represents a conceptual synthesis of what has been shown through many different types of direct and indirect experimentations, enabled by the evolving experimental tools available to developmental biologists. Transplantation technology allowed the astounding discovery of the developmental organizer,[1] mutagenesis uncovered many key developmental genes/networks and their roles,[2,3] genomic sequencing revealed unexpected levels of evolutionary conservation in the development of the animal body plan,[4,5] and the discovery of fluorescent proteins[6,7] has enabled the construction of genetic reporters for labeling and tracking specific populations of cells in developing embryos.[8] These discoveries have helped us to understand the origin of birth defects,[9,10] the interplay of genetic and environmental factors during development,[11–13] and how to genetically program clinically important cell types for regenerative therapies.[14–16] The foundation of this process of discovery is visualization, a function of contrast mechanisms and the ability to meaningfully capture them. Consequently, the progress in understanding embryonic development and downstream clinical application of that basic knowledge is intimately tied to the progress in imaging technology.

To emphasize the demands on an imaging system that would attempt to directly capture them, the events of embryonic development can be briefly summarized as follows. When an egg (a zebrafish egg of approximately 700 μm in diameter[17,18]) is fertilized, the resulting embryo begins a stage of rapid cell division (15 to 30 min per division[19]), known as the cleavage stage. Toward the end of this stage, the embryo transits from relying on pre-existing molecular cues deposited in the egg to utilizing its own genomic machinery (thousands of genes[20,21]) and shortly thereafter, the three germ layers are distinguished during the process of gastrulation, where rapid cell movements (few μm/min[22]) accompanied by spatiotemporal varying patterns of gene expression result in recognizable anterior-posterior and dorsal-ventral embryonic axes. Continued cell proliferation, slowed cell movements ($\sim$0.5 μm/min[22]), and further refinement of gene expression shape the body plan composed of segments of appropriately fated cell lineages (now tens of thousands of cells[22]). From this point, within each segment cells differentiate and take on specific morphologies and functions, as individual organs mature. Perhaps not surprisingly, despite a detailed framework and list of components, these events as a whole have yet to be fully observed or understood.

Each aspect of embryonic development, then, presents unique challenges. Its dynamism requires imaging to be nondestructive and preferably noninvasive. Its fundamental unit is the cell, but subcellular events, such as cell division and

mitotic spindle orientation, are vital to proper embryonic development, as they are collective cell behaviors behind tissue and organ morphogenesis. Adding to the complexity is the daunting number of involved genes that have disparate spatial and temporal expression patterns. All this activity occurs over a relatively large three-dimensional (3-D) space, placing further demands on imaging capabilities. The challenge to modern imaging systems, then, is to rapidly and noninvasively acquire large, high resolution, multichannel volumetric images from a live developing embryo.[23]

Toward this goal, two-photon microscopy (2PM) has become favored over one-photon approaches because of the advantages of near-infrared (NIR) light, including (1) less photodamage to embryos, allowing longer time-lapse imaging sessions, (2) less scattering, allowing deeper imaging into embryos, especially more opaque embryos, and (3) the option of simultaneously exciting multiple fluorescent species in the biological window (near IR), without the excitation light (750 to 1000 nm) interfering with imaging signals (400 to 700 nm).[24] As 2PM techniques have become more widespread, so has ultrafast laser technology, with most imaging systems typically employing pulses from a Ti:Sapphire oscillator with a temporal duration of 100 to 170 fs.[25,26] Despite the advantages gained by adopting 2PM, however, it has remained challenging to acquire high-resolution, 3-D multichannel movies of embryonic development.

Microscopists are well acquainted with the trade-offs encountered when attempting to optimize imaging parameters due to a photon economy, i.e., limited by the organism's tolerance of the probing light radiation. For example, to increase imaging speed to capture more rapid cell movements during embryogenesis, narrowband NIR pulses will generally be tuned to the optimum 2P absorption peak of a single-fluorescent marker and all emitted light will be collected as a single channel.[27] This approach provides "in toto" characterization of cell proliferation, death, and migration, but provides little information about the shaping of the embryonic tissue and none about the genetic specification of cells. With a transition from single-point scanning to line scanning, the excitation light source, as in digital scanned light-sheet microscopy (DSLM), can possibly add another channel.[28,29] However, imaging two or three genetic markers in four-dimensional (space, time) are the current technological limit,[27,30] while the genetic regulatory networks governing embryonic development contain vastly more components.

Optical coherence tomography/microscopy (OCT/M) is a linear imaging technique that images the morphology of biological samples based on changes in index of refraction that frequently employ NIR laser pulses.[31] Because of the high sensitivity of the interferometric detection scheme employed in OCT/M, this approach has been used to image extraordinarily fast movements during embryogenesis such as heart tube pumping and development.[32,33] Alternatively, because of the enhanced penetration of both the input and output NIR signals, OCT has also been used for longitudinal imaging of mouse embryos *in utero*, where the uterus is temporarily dissected from the mother.[34,35] Since 2PM and OCT/M can be relatively easily integrated into a multimodal platform, it would be interesting to explore potential applications of OCT/M to additionally render molecularly specific signals in the context of embryonic development.

NBT/BCIP is a robust and strongly scattering precipitate that is commonly used to mark domains of gene expression through a standard immunohistochemical technique called *in situ* hybridization (ISH).[36] Though ISH requires embryos to be fixed, it provides fundamentally unique data from 2PM approaches that track fluorescent protein markers because it provides a more accurate view of gene transcript localization at a specific developmental stage. Such data will be complementary to that obtained by time-lapse 2PM, while also being relatively easily obtained with the same imaging platform.

Here, we present the theoretical benefit of using ultrashort pulses, on the order of 10 fs, for imaging embryonic development and demonstrating the benefit manifest such as unique capabilities for exciting and rendering a wide variety of optical signals from developing embryos simultaneously. In addition, we demonstrate these capabilities in a system, where dispersion compensation is implemented in a relatively simple and user-friendly manner using double-chirped mirrors.[37] Our multimodal instrument can be used for 2PM (and other forms of nonlinear optical microscopy such as second-harmonic generation) with standard two-channel detection or with spectral detection, as well as for OCM, and we refer to these techniques collectively as ultrashort pulse microscopy (UPM). Within a single experiment, UPM provides the opportunity to better link the behaviors of genetically labeled cell lineages with the morphogenesis of tissues and organs during development. In addition, while UPM still only scratches the surface of embryonic development in its entirety, it does have the potential to provide more information from a single experiment than other approaches, which could enable a more accurate construction of systems-level views of vertebrate development by a combination of datasets onto dynamic digital atlases.[38–40]

2 Theory

For imaging embryonic development, ultrashort pulses provide the unique capabilities of simultaneous excitation of a broad range of fluorophores and a short coherence gate for high-resolution optical coherence microscopy of tissues or deposited scattering precipitates.

2.1 *Two-Photon Excitation by Ultrashort Pulses*

Temporally ultrashort pulses, such as in the 10-fs regime, are advantageous compared with conventional 100 to 170-fs pulses used in 2PM applications, because (1) for a given pulse energy, the peak power of an ultrashort pulse will be higher because the energy is compressed in time, and (2) an ultrashort pulse necessarily contains a broader range of wavelengths that can together create two-photon transitions.[41,42] Using a semi-classical model of a two-photon transition, where the electric field is treated classically and the molecule is treated quantum mechanically as a two-level system, this benefit can be quantified in terms of relative two-photon transition probabilities.

To compare the theoretical transition probabilities of our sub-10-fs pulses with conventional pulses, we first measured the spectral intensity, $|E(\omega)|^2$, of sub-10-fs pulses output from our Ti:Sapphire oscillator. To model the electric field, $E(\omega)$, of alternative transform-limited pulses (all frequencies arrive at the focus in phase) of varying temporal

durations, τ_p, we used the Gaussian relationship shown in Eq. (1).

$$E(\omega) = \exp[-\tau_p^2 \omega^2 / 8 \ln(2)]. \qquad (1)$$

Two-photon transitions can occur through degenerate and nondegenerate mixings of frequency components, so if the pulse is transform limited, then all possible combinations of the frequencies within the pulse can be given by the two-photon excitation power spectrum,[43] $T(\omega)$, which is described by Eq. (2).

$$T(\omega) = \left| \int_0^\infty E\left(\frac{\omega}{2} + \Omega\right) E\left(\frac{\omega}{2} - \Omega\right) d\Omega \right|^2. \qquad (2)$$

The two-photon excitation spectrum of our sub-10-fs pulse is compared with that of a 100-fs pulse in Fig. 1(a). In the context of imaging embryonic development, molecules of interest generally have a frequency-dependent response, sometimes called a two-photon action cross-section.[44] To meaningfully compare the theoretical performance of these pulses, this response must be known. The yield or transition probability,[45,46] Γ, is then the overlap integral of $T(\omega)$ and the frequency response of the molecule, $\gamma(\omega)$, as shown in Eq. (3).

$$\Gamma \propto \int_{-\infty}^\infty T(\omega)\gamma(\omega) d\omega. \qquad (3)$$

From Eq. (3), it can be seen that the probability of a two-photon transition depends on the magnitude of the area under the two-photon power spectrum curve and the degree to which this overlaps with the absorption lineshape of a given fluorophore. We used $\gamma(\omega)$ measured from the commonly used enhanced green fluorescent protein (eGFP)[47] to calculate transition probabilities for our sub-10-fs pulses centered at 800 nm and for 100-fs pulses centered at 940 nm, the maximum of the eGFP frequency response, illustrated in Fig. 1(b). We calculated a fivefold enhancement of yield in

the case of un-tuned, sub-10-fs pulses compared with optimally tuned 100-fs pulses given the same pulse energies. In terms of imaging embryonic development, this enhancement could be used to image more rapidly or, alternatively, to decrease pulse energy to reduce stress on the developing embryo.

For imaging multiple fluorescent protein variants simultaneously, the advantage of using sub-10-fs pulses increases. A single narrowband source will necessarily be tuned to a compromised wavelength that interacts with the frequency responses of the different molecules, decreasing the yield for each, while the sub-10-fs pulse interacts substantially with each simultaneously.[48,49] Thus, with ultrashort pulses, it may be more feasible to image multiple genetically marked lineages during embryonic development.

2.2 Coherence Gating with Ultrashort Pulses

The benefits of utilizing the short coherence length of ultrashort pulses to improve axial resolution of OCT/M are well known.[50] Using Fourier-domain detection, the frequency components of the interferogram produced by the sample and reference arms encode the spatial profile of the biological sample along the optical axis (A-line), within the confocal parameter of the imaging objective.[51] Rapid 3-D imaging can be achieved by scanning this A-line across the sample in two dimensions. Thus, for OCT imaging, a low-numerical aperture (NA) objective resulting in a large depth of field is desirable, as long as the diffraction-limited lateral resolution remains comparable with the axial resolution, Δz,[51,52] which depends on the source bandwidth at full-width-half-maximum (FWHM), as shown in Eq. (4).

$$\Delta z = \frac{2(\ln 2)}{\pi} \frac{\lambda_0^2}{\Delta\lambda}. \qquad (4)$$

Our sub-10-fs pulses have a FWHM of $\Delta\lambda = 133$ nm centered at $\lambda_0 = 800$ nm corresponding to a theoretical axial resolution of 2.12 μm, whereas a more conventional pulse with a bandwidth of 10 nm at this central wavelength will
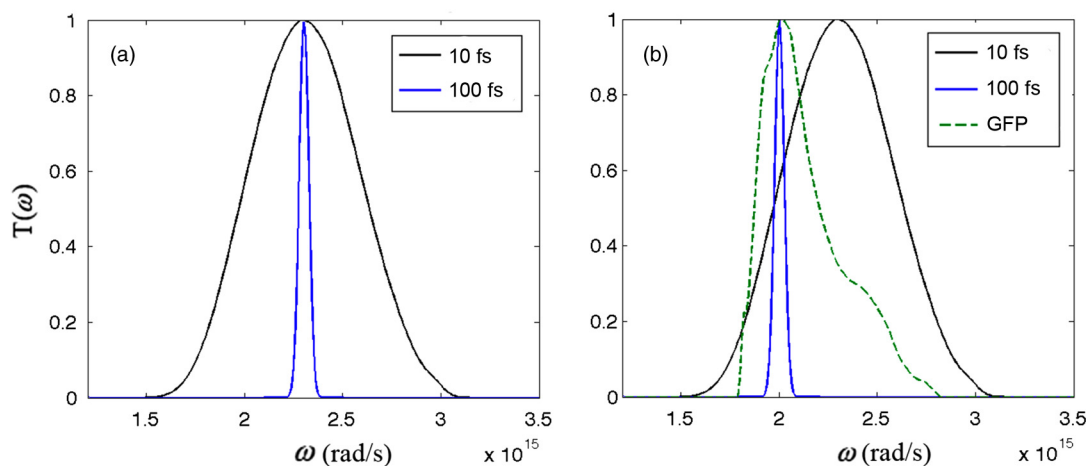

Fig. 1 Advantage of using ultrashort pulses in two-photon microscopy (2PM). (a) Two-photon power spectra, $T(\omega)$, for 10 fs (black line) versus 100 fs (blue line) pulses with the same pulse energy centered at 800 nm. The area under the curve represents the ability to create two-photon transitions in materials with frequency-independent response, $\gamma(\omega)$. (b) $T(\omega)$ for 10 fs (black line) pulses at 800 nm and 100 fs pulses (blue line) tuned to 940 nm, the maxima of $\gamma(\omega)$ for green fluorescent protein (GFP) (dotted green line). The ability to create two-photon transitions for GFP, where the response is now frequency dependent, is the overlap integral of $T(\omega)$ and $\gamma(\omega)$, which is five times greater in the case of untuned, transform-limited pulses at 10-fs pulses at 800 nm versus optimally tuned 100-fs pulses.

have an axial resolution of 28 μm. This resolution difference is significant when imaging individual cells and small-scale tissue structures in developing embryos. In the context of combining OCM with 2PM, the resolution offered by the use of ultrashort pulses also better matches the two-photon interaction volume resulting from a tightly focusing high NA objective, so simultaneously acquired 2PM and OCM images are co-registered.[53]

3 Methods

3.1 Instrumentation

Our multimodal UPM system, summarized in Fig. 2, combines 2PM and Fourier-domain OCT/M in a single platform with the option of either two-channel (with OCM) or spectral detection (stand alone) capabilities for 2PM. Detailed more in these reports,[37,53,54] we describe the instrument here briefly. The sub-10-fs pulses from a Kerr-lens mode-locked Ti:Sapphire oscillator (Femtolasers, Vienna, Austria) at a 800-nm central wavelength with 133-nm bandwidth (FWHM) are precompensated using double-chirped mirrors (GSM 270, Femtolasers) and coupled to the multimodal imaging system. For combined 2PM-OCM, a 5% beamsplitter splits the beam into signal and reference arms in a Michelson interferometer configuration. The signal arm is coupled using galvanometer-driven mirrors (Cambridge Technology, Cambridge, Massachusetts) into an upright microscope (Axioskop2, MAT, Carl Zeiss, Thornwood, New York), expanded, and directed by a 635-nm short-pass dichroic mirror (Chroma Technologies, Bellows Falls, New York) to the back aperture of the water-immersion imaging objective (20×, 1.0 NA or 40×, 0.8 NA, Carl Zeiss), which focuses the pulses to a diffraction-limited spot that is scanned in the x-y plane across the sample. The backscattered near-infrared light is collected by the imaging objective and reflected back to the beamsplitter, where it recombines with the reference arm and is coupled into a single-mode fiber and sent to a home-built spectrometer consisting of a collimating lens, reflective grating (1200 lines/mm), focusing lens, and CCD array (Basler, Exton, Pennsylvania). Dispersion is matched in the reference arm using a combination of a prism pair and BK7 glass. For OCM, the interferogram obtained from each pixel is integrated into a single intensity value to build up a 256×256 two-dimensional (2-D) image rendered en face. Simultaneously, 2PM signals are collected by the imaging
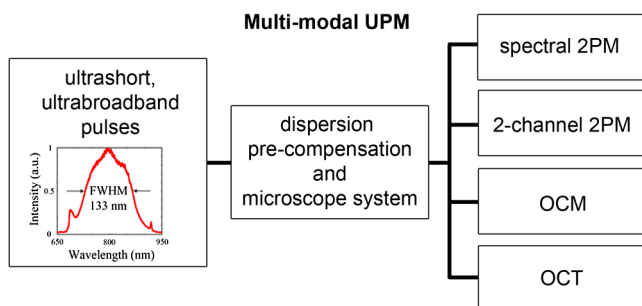
objective and directed onto the two PMT detectors (Hammamatsu, Bridgewater, NJ) using appropriate dichroic mirrors and bandpass filters (Chroma). Photon counts are saved as intensity values.

For spectral 2PM, the 2PM signals are collected by the imaging objective, coupled into a multimode fiber, and sent to a home-built spectrometer consisting of a collimating lens, diffraction grating (700 lines/mm), focusing lens, and a 16-channel multianode PMT array (Hammamatsu). The 3-D images are built up by translating the sample in the z-direction along the optical axis. Instrumentation control and data acquisition are performed using custom LabVIEW software (National Instruments, Austin, Texas).

3.2 Label-Free Imaging of Fixed and Live Wild-Type Embryos

Zebrafish were maintained and bred according to the standard protocols.[55] For imaging, wild-type embryos were treated with 0.003% (w/v) phenylthioluria, to suppress the formation of pigment cells (except for label-free imaging of melanocytes), and mounted in 1.2% low-melt agarose hydrated with Instant Ocean (United Pet Group, Blacksburg, VA). Live wild-type embryos were imaged at 25°C with time-lapse imaging performed at 27°C for 15- to 30-min intervals. In some cases, embryos were fixed in 4% (w/v) paraformaldehyde overnight at 4°C and stored in phosphate-buffered saline (PBS) before imaging. Average power of the excitation beam was attenuated to 25 to 30 mW on the sample (not accounting for scattering due to the agarose embedding) and pixel dwell time ranged from 120 to 480 μs. In most cases, lateral resolution was limited by digital resolution but kept to the order of 1 to 2 μm, while axial step size was generally 3 μm, as recommended by Keller et al.,[22] to capture all cells in the imaging volume. Signals were collected into a single channel using a BG39 filter (Schott, Elmsford, NY).

3.3 Imaging Transgenic Embryos

Stable transgenic lines expressing eGFP under a wnt1 regulatory element that recapitulates wnt1 expression in the midbrain and at the midbrain-hindbrain boundary (Lilie et al., unpublished) were used to demonstrate time-lapse imaging of genetically labeled cell lineages in live zebrafish embryos. Transgenic fish were intercrossed, and embryos were imaged during the segmentation period of development as described above, with stacks acquired at 15-min intervals. Autofluorescence and eGFP signals were separated with a 490-nm long-pass dichroic mirror (Chroma) and further discriminated with 450/60 and 525/50 nm band-pass filters (Chroma), respectively. For demonstrating excitation and spectral detection of a variety of fluorescent protein variants within zebrafish embryos using ultrashort pulses, wild-type embryos were injected at the one-cell stage with plasmid DNA containing a fluorescent protein gene (eBFP2, CFP, mOrange, and mRFP) or a fluorescent protein fusion (citrine-H2B) under a cmv promoter, resulting in mosaic expression throughout cells of the embryo at 24 hours post-fertilization (hpf). For acquiring spectral images of eGFP, the aforementioned stable transgenic lines were used. Embryos were imaged at 24 hpf, and fluorescent signals were collected with the spectral detection scheme described in Sec. 3.1.

Multi-modal UPM

ultrashort, ultrabroadband pulses

Intensity (a.u.)

FWHM 133 nm

650 800 950
Wavelength (nm)

dispersion pre-compensation and microscope system

spectral 2PM

2-channel 2PM

OCM

OCT

Fig. 2 Multidoal ultrashort pulse microscopy (UPM). A single oscillator outputting 10-fs pulses centered at 800 nm at 75 MHz is coupled to a microscopy system with several detection modes. Pulses are precompensated for dispersion introduced by the microscopy system with double-chirped mirrors.

3.4 In Situ Hybridization and Imaging NBT/BCIP with 3-D Resolution

The ISH was performed as previously described[56] for either *krox20* or *egfp* mRNAs. Embryos stained with NBT/BCIP and hydrated in PBS were mounted as described above and imaged in the combined 2PM-OCM modality with an average power of 35 mW on the sample (not accounting for scattering due to the agarose embedding), a pixel dwell time of 480 μs, and a step size of 3 μm.

3.5 Image Processing

Images were processed using custom MATLAB routines and openly available image-processing software ImageJ and FIJI.[57] 3-D multichannel reconstructions were rendered in V3D.[58] Nuclear segmentation from autofluorescence signal was performed manually.

Spectral unmixing was performed with custom MATLAB routines that utilized spectral standards of the components to be unmixed (obtained online from Invitrogen and Molecular Probes or measured experimentally). The algorithm creates a set of fits, $F(\lambda)$, that are the linear-weighted sum of n scalar coefficients, c_i, and 16-element reference spectra, $R_i(\lambda)$, of n presumed constituents, as shown in Eq. (5)

$$F(\lambda) = \sum_{i=1}^{n} c_i R_i(\lambda). \tag{5}$$

The solution is the set of positive coefficients that sum to 1 and produces a fit that minimizes the mean squared error between the fit and measured spectra.

4 Results and Discussion

4.1 Label-Free Imaging of Embryonic Tissues

To determine whether endogenous fluorescence could be used to image vertebrate development, we imaged wild-type zebrafish embryos free of exogenous labels with 10-fs pulses centered at 800 nm. The zebrafish, also known as *Danio rerio*, is a well characterized and established model organism, especially useful for time-lapse imaging analysis of developmental mechanisms.[17]

We first examined embryonic development at the tissue level. At 24 hpf, the major organ systems in zebrafish embryos have taken on a recognizable morphology according to the basic vertebrate body plan, so we imaged a fixed embryo in its entirety using overlapping fields of view to observe those features visible from endogenous fluorescence. The combined image rendered using FIJI volume viewer is shown in Fig. 3(a).

We observed a strong autofluorescence signal from most of the tissues in the embryo, and developing structures were easily visible in optical sections, including structures of the eye, ear, developing brain and ventricular system, notochord, blood islands, and muscle segments [Figs. 3(b)–3(f)]. These data illustrate that ultrashort pulses efficiently excite autofluorescence from the constituent cells of the embryo, such that the morphogenesis of a wide variety of organ systems can be characterized quantitatively without the need for exogenous labels. Such data will be useful for the re-emerging field of physical biology that seeks to model the mechanical forces that give rise to embryonic shape[59,60]
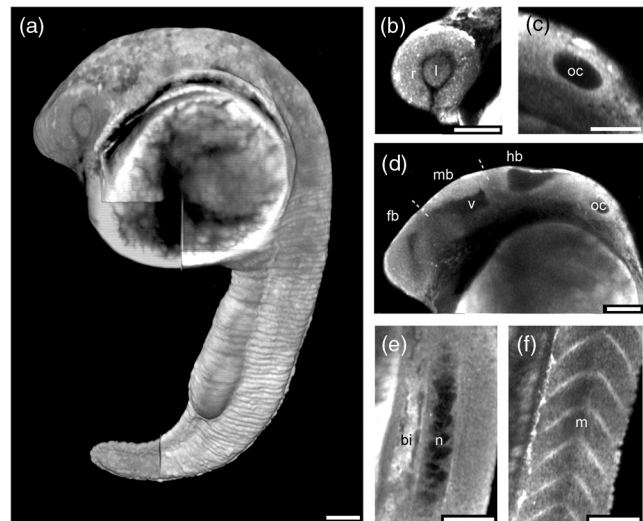

Fig. 3 Label-free imaging of embryo and organ morphology with UPM. (a) Lateral view of a volume rendering of endogenous signals excited by ultrashort pulses in a zebrafish embryo at 24 hours post fertilization (hpf), also referred to as the prim-5 stage. Image is the product of fusing nine different volumes. (b–f) Optical sections of the same embryo detailing various forming organs including (b) the eye, composed of the lens (l) and retina (r), (c) the developing otic cup (oc), (d) different brain segments, including the forebrain (fb), mid-brain (mb), and hindbrain (hb), and ventricular spaces (v), (e) trunk region including notochord (n) and blood islands (bi), and (f) more laterally in the trunk region, myotome (m) or muscle segments. Scale bars are 100 μm.

and potentially connect these forces to specific cell behaviors and patterns of gene expression.

4.2 Label-Free Imaging of Individual Cells and Their Movements

We were also interested to determine whether cellular auto-fluorescence signal was sufficient for tracking individual cells; so, we performed time-lapse imaging of the cranial region of zebrafish embryos during the segmentation period when neural crest cells are derived from the roof plate of the neural tube and migrate to give rise to different structures and cell types in the embryo including craniofacial cartilage and bone, melanocytes, and peripheral sensory neurons.[61] As seen in Figs. 4(a) and 4(b), these neural crest cells generally originate from the dorsal side of the densely packed neuroepithelium and migrate laterally and ventrally into a less-dense mesenchyme outside the neural tube. In this mesenchyme, individual neural crest cells were easily visible from autofluorescence signal and demonstrate that UPM could potentially be utilized to track the dynamic migration of different populations of neural crest, i.e., produce a high-resolution neural crest fate map independent of exogenous cell labels.

We also decreased the field-of-view to match our digital resolution to the diffraction-limited performance of the system and to assess the possibility of imaging individual cells within the tightly packed neuroepithelium at 24 hpf. At this time in development, the neuroepithelium is a contorted tube, highly stratified in the apical side in contact with the brain ventricular system and the basal side facing outward. Figure 4(c) shows a cartoon of this arrangement from a dorsal view, where the anterior portion of the head is directed to
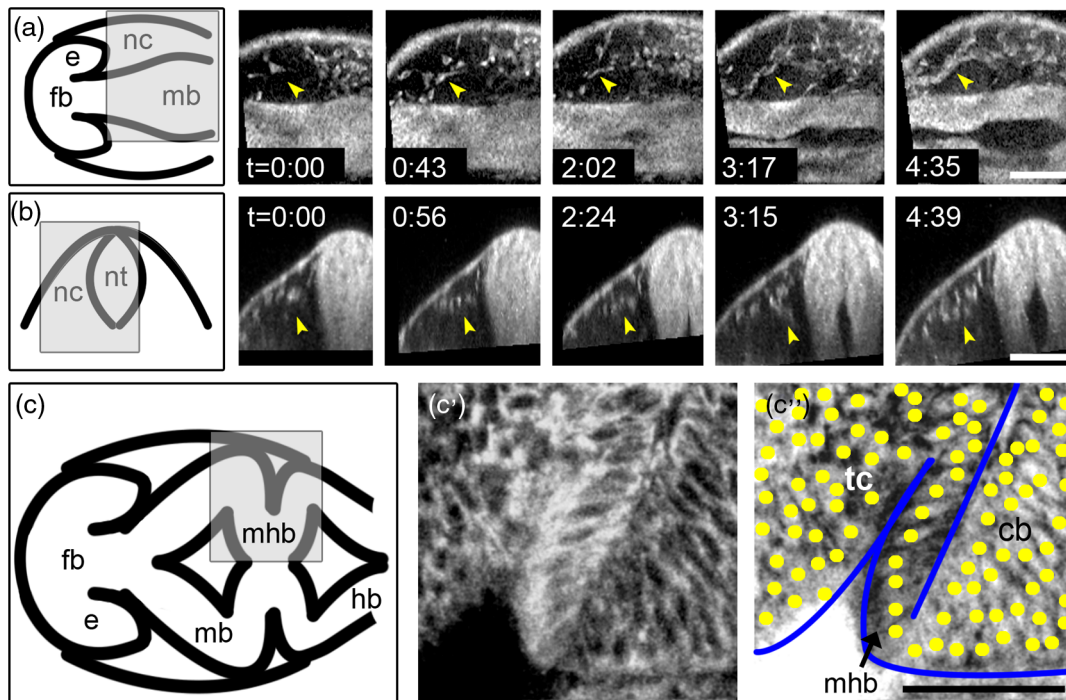
Fig. 4 Label-free imaging of individual cells and their movements with UPM. (a) For reference, a cartoon of a dorsal view of the embryonic brain including the forebrain (fb), eye (e), neural crest (nc), and midbrain (mb). Left–right symmetry can be assumed. The rest of (a) are the optical sections (x, y) depicting coordinated migration of neural crest cells in a low-density mesenchyme tracked during the segmentation period of development ($t = 0{:}00$ is the 10 somite stage). Images were rendered *en face* in this orientation. (b) Cartoon depicting a transverse view of the embryonic neural tube (nt). The rest of (b) are the optical sections (y, z) of neural crest cells migrating lateral to the neural tube. (c) Cartoon depicting morphology of the midbrain-hindbrain boundary (MHB) at 24 hpf. (c') Optical section of the area outlined in gray. At this stage, the neuroepithelium is stratified and densely packed, but autofluorescence excited by ultrashort pulses can still be used to identify individual cells. Nuclei, lacking endogenous fluorophores, remain dark. (c") Different cellular organizations in different brain compartments, such as the tectum (tc) and cerebellum (cb), including a special nonstratified epithelium at the MHB. Scale bars are 100 μm.

the left. The neural tube has been segmented into morphologically distinct regions including the forebrain (fb), midbrain (mb), and hindbrain (hb). The boundary between the midbrain and hindbrain is referred to as the midbrain-hindbrain boundary (MHB) organizer [the term organizer denotes the importance of this region for correct development of structures in the midbrain and hindbrain such as the tectum (tc) and cerebellum (cb), respectively]. Figure 4(c)' shows autofluorescence from an optical section taken from this boundary region on the right side of the embryo. The large dark portion of the image in the bottom left corresponds to the fluid-filled brain ventricle, whereas the other dark spots correspond to individual cell nuclei. Figure 4(c)" is the same image inverted and marked to show the arrangement of individual cell nuclei in yellow and the outline of the neuroepithelium in blue. We were able to image a unique region of the epithelium at the boundary, where a group of cells seems to have recaptured the character of a simple one-layer epithelium with the nuclei aligned rather than staggered. This particular arrangement may provide some structural support to the MHB constriction, as the tectum and cerebellum rapidly develop on either side. We have also observed that this group of cells can be identified by their strong expression of *wnt1* (Figs. 6 and 8). While there is a significant literature concerning the genetic basis underlying the structure and specification of this region,[62,63] there is relatively little known concerning details about how these genes direct individual or collective cell behaviors that achieve this complex tissue architecture.

The autofluorescence signal we detect arises predominantly from pyridine nucleotides and flavins found in the mitochondria and cytoplasm, whose 2P excitation spectra have been measured.[64] While narrowband pulses can simultaneously excite key autofluorescence molecules NADH, NAD(P)H, FAD, and lipamide dehydrogenase, we have not seen reports of these signals used to measure tissue morphology and cellular movements over time in embryonic development. It may be that for a given pulse energy, ultrashort pulses provide a significant enhancement over conventional pulses such that the autofluorescence is transformed from unwanted background noise to a label-free method to integrate the cellular and tissue scale dynamics of development.

4.3 Label-Free Imaging of Pigmented Cells

Melanocytes, derived from the multipotent neural crest cell lineage, have been a prominent model for the study of cell differentiation and establishment of adult stem cell populations during development.[65] We have observed strong (up to 10-fold stronger than cellular autofluorescence) 2P excited fluorescence from melanocytes (commonly called melanophores in fish), as shown in a volumetric maximum intensity projection in Fig. 5(a). Live embryos that were not treated to block melanin production were imaged at 24 hpf. We observed brightly fluorescing cells distributed throughout the cranial region underneath the periderm displaying expected differentiated cranial melanocyte morphology
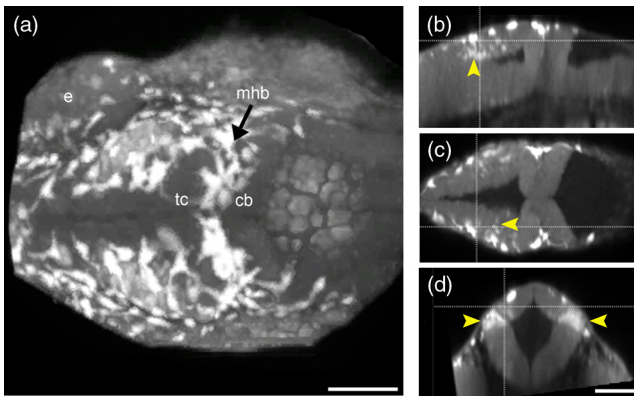
Fig. 5 Label-free imaging of melanocytes and other pigment cells. (a) Dorsal view of a three-dimensional (3-D) maximum intensity projection of the embryonic zebrafish brain at 24 hpf. At this stage, cells derived from the neural crest have differentiated into melanocytes in a characteristic pattern in the cranial region. A strong signal (10-fold brighter than tissue autofluorescence) excited by ultrashort pulses matches this characteristic pattern. (b–d) Optical sections (b—lateral, c—dorsal, and d—transverse) from volume in (a) also reveal a population of pigmented cells in the neural epithelium that is localized at dorsolateral hinge points in the tectal primordium. Cells appear to be undergoing an epithelial-to-mesenchyme transition. Scale bars are 100 μm.

and positioning.[61,65] Neural crest delamination and migration occur with varying dynamics along the anterior-posterior axis and, at a specific spatial location, neural crest may delaminate in temporally sequential waves. For example, in the zebrafish trunk, at least two different temporal waves give rise to neural crest migration along a medial and, later, a more lateral pathway.[66] In the cranial region, these dynamics are not well characterized and could be significantly more complex.

Optical sections in Figs. 5(b)–5(d) reveal a striking population in the optic tectum localized at the dorsolateral hinge points of the neural tube, which appear pigmented while still integrated in the neural epithelium. This finding is unusual, because melanocytes are generally thought to differentiate from melanoblast precursors that have already delaminated from the neuroepithelium.[67] Some neurons, such as dopaminergic neurons, are known to be pigmented,[68] but no pigmented neurons have been reported in this region of the optic tectum in zebrafish. One interpretation of this data is that ultrashort pulses provide significantly more sensitive detection of melanin than can be achieved with standard light microscopy and that, at least for a subpopulation of melanocytes, differentiation occurs prior to or during the epithelial-to-mesenchyme transition. Efficient 2P excitation of melanin using conventional pulses and resulting in bright fluorescent signals has been reported in cell culture[69] and in a concentration-dependent manner *in vivo*.[70] It would be interesting to use a combination of autofluorescence and melanin fluorescence to track the origin and eventual fate of this unique population, although the overwhelming melanin signal may impede the addition of any fluorescent protein gene reporters simultaneously.
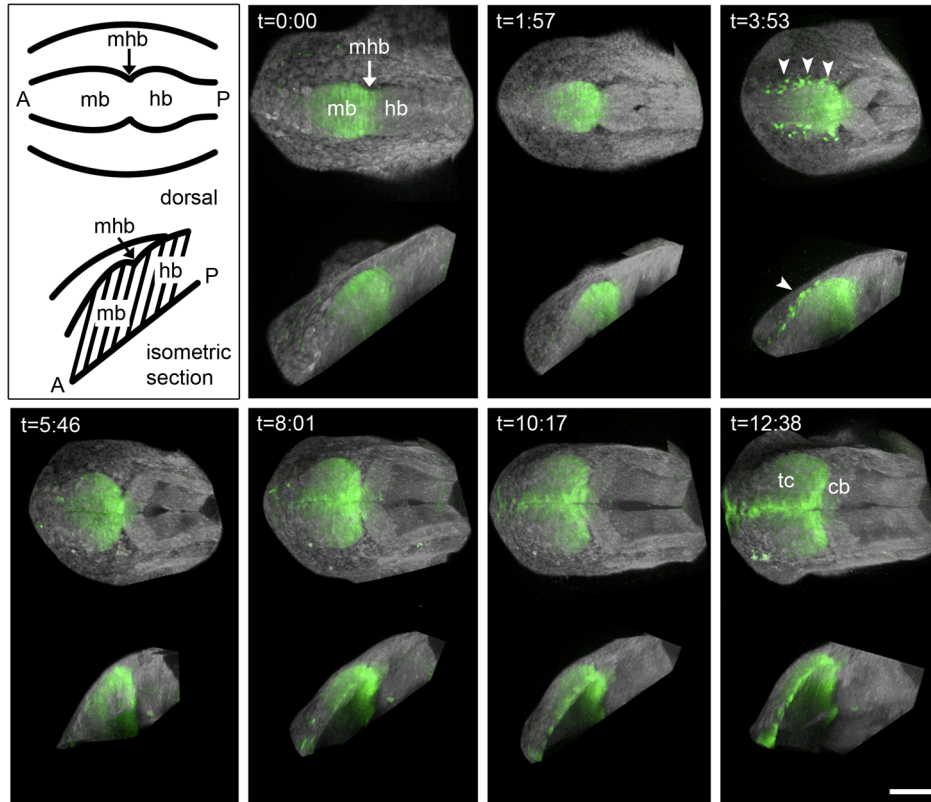
4.4 Time-Lapse Imaging of Genetically Labeled Cell Lineages

We next demonstrated the imaging of the dynamics of a genetically labeled cell lineage simultaneously with

morphogenetic events in the embryonic brain. Stable transgenic embryos expressing eGFP under the control of regulatory elements from the *wnt1* gene were imaged during segmentation over a period of 12 to 13 h. During segmentation, *wnt1* is expressed in the midbrain and at the MHB and is important for proper development of the region. In mice lacking Wnt1, the entire midbrain and hindbrain regions (known as mes/r1) are deleted.[71] In zebrafish, other Wnts have redundant roles to *wnt1*; however, loss of these Wnts in combination also results in the deletion of midbrain and hindbrain structures.[56,72] Thus, *wnt1* has an important role in the specification of these embryonic brain tissues.

Morphogenesis of the MHB region imaged with UPM progressed in step with previous reports.[73,74] We show in Fig. 6 the dynamics of the *wnt1*-expressing lineage in this complex structural environment of the mes/r1 region. When the MHB is initially formed, genetic determinants from either side of the boundary initially overlap, and subsequently their expression sharpens.[63] This sharpening coincides with the development of a morphologically visible constriction at the boundary by the 10-somite stage ($t = 0\!:\!00$). We observe eGFP positive cells in the hindbrain at this stage whose fluorescence gradually diminishes, suggesting that the boundary sharpens at least in part when cells alter their pattern of gene expression in response to a still undetermined mechanism of spatial identity acquisition. At $t = 0\!:\!00$, we also observe the *wnt1* lineage to have a longer extent along the anterior-posterior axis in the dorsal neural tube than in ventral neural tube and find that this arrangement persists throughout the periods of segmentation and ventricle formation, suggesting that this initially labeled lineage is proliferative but relatively stationary along the anterior-posterior axis within the neuroepithelium. Intensity of the eGFP signal increases over time in cells at the boundary itself and anteriorly along the dorsal midline up to the epiphysis, indicating continuous production of reporter transcripts in these regions, which maintain *wnt1* expression. At $t = 3\!:\!53$, we also captured the epithelial-to-mesenchyme transition of a portion of the *wnt1* lineage comprising neural crest cells, marked by arrowheads. After the time-lapse imaging concluded, we observed disfiguration of the tail and slight edema as expected when immobilizing zebrafish embryos with a combination of tricaine and agarose,[75] but otherwise embryos continued to develop normally through larval stages.

Photobleaching by ultrashort pulses appears to be minimal as subpopulations of the *wnt1* lineage that have stopped transcribing the *wnt1* reporter (as indicated by ISH at previous stages) can be tracked for several hours, despite the dilution of available eGFP molecules by cell division. As mentioned previously, ultrashort pulses do not appear to cause undue stress to the developing embryo as evidenced by normal morphological progression of the irradiated region of the embryo throughout the period of imaging and up to 7 days later. However, in the future, it may be prudent to assess the damage threshold for these organisms using ultrashort pulses similar to what has been reported for *Drosophila*.[76] Using a combination of markers, including lethality, necrosis, and TUNEL staining, Saytashev et al. showed that for a given signal level, shorter pulses (37 fs) resulted in less thermal damage and fewer DNA strand breaks than longer pulses (100 fs).

Fig. 6 Imaging genetically labeled cell lineages in their morphological context. First panel shows a cartoon of the region of the brain depicted in subsequent 3-D maximum intensity projections from a time-lapse experiment on a stable transgenic line expressing eGFP protein under the control of a *wnt1* regulatory element. Time-lapse follows the midbrain (mb) and hindbrain (hb) regions during the formation of the midbrain-hindbrain boundary (MHB) constriction and brain ventricle formation. $t = 0:00$ corresponds to the 10 to 12 somite stages, when the neural tube is still closed. The *wnt1* population (green) is tracked with 3-D resolution alongside the dramatic reorganization of neural morphology visible by autofluorescence (white). Arrows point to the migration of neural crest cells that are derived from a *wnt1* lineage. Scale bar is 100 μm.
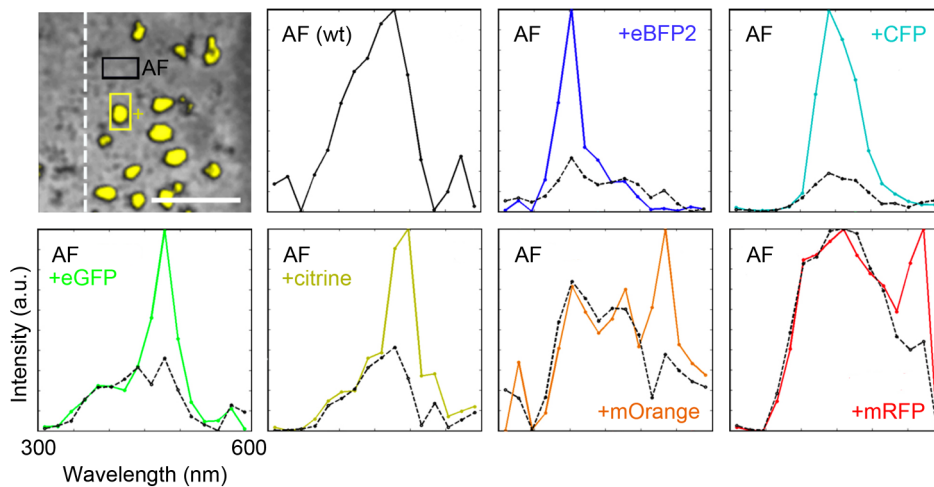
Fig. 7 Excitation and spectral detection of fluorescent protein variants transiently expressed in zebrafish embryos. First panel shows a representative image from an embryo mosaically expressing a fluorescent protein variant (citrine-H2B, in this case, segmented and superimposed in yellow). Dotted line represents the embryonic midline, and boxes show areas from which pixel-by-pixel 16-channel spectra have been summed. Subsequent graphs show the spectral data from embryos injected with different variants, spanning a range from blue to red fluorescent proteins. One spectral profile obtained from a region of the embryo with little or no exogenous label (black line) is compared with an area where the injected fluorescent protein is present (appropriately colored line). The autofluorescence (AF) contributes a broad and somewhat indistinct spectral profile, while peaks from individual fluorescent proteins are readily identifiable at their expected locations. Scale bar is 50 μm.

### 4.5 Imaging a Variety of Labels with a Single Pulsed Source

To demonstrate the potential for capturing the dynamics of multiple fluorescently labeled genetic lineages simultaneously during embryonic development, we obtained several fluorescent protein (FP) variants and expressed them mosaically in independent zebrafish embryos through transient transgenesis. These embryos were imaged at 24 hpf using our home-built 16-channel spectral detector, spanning 350 to 630 nm for capturing 2P-excited fluorescence signals. For each pixel in a 2-D image or voxel in a 3-D image, a 16-channel lambda stack is acquired from live embryos. The average of the spectral profile for different regions in the embryos, as shown in Fig. 7, was compared with delineated autofluorescence contributions (acquired from areas of the embryo not expressing the injected fluorescent protein variant) and spectral signatures from eBFP2, CFP, eGFP, citrine, mOrange, and mRFP. Except for eGFP, the amount of plasmid injected was the same for each FP variant, and thus, the relative intensity of fluorescent protein to autofluorescence can be interpreted using the 2P overlap integral among the variants with our two-photon excitation power spectrum, as in Eq. (3). As expected, for pulses centered at 800 nm, the overlap appears to be more significant for blue variants than for red, although the other red variants such as TagRFP1[77] have been reported to have a significant 2P action cross-section near 800 nm and, thus, may be better suited for this application. These spectral signatures show that we can indeed efficiently excite a wide spectrum of fluorescent protein variants simultaneously, as all spectra were obtained with the same untuned ultrashort pulses. Once a suitable transgenic line is created, it may be then possible to image the dynamics of up to five different genetically labeled lineages.

To demonstrate the potential to accurately delineate these simultaneously excited overlapping spectral emissions, we performed spectral time-lapse imaging with simultaneous excitation of closely overlapping eGFP and citrine (a yellow fluorescent protein) emissions and separated them with linear unmixing. The unmixing algorithm assumed three constituents: (1) autofluorescence, (2) eGFP, and (3) citrine. Autofluorescence reference spectra were measured directly from wild-type embryos, whereas eGFP and citrine reference spectra are available online (Molecular Probes and Invitrogen). The stable transgenic line marking the *wnt1* lineage with eGFP was injected with plasmid DNA encoding citrine-H2B at the one-cell stage, resulting in differential distribution of these two fluorescent markers across the MHB at 24 hpf. Summed images are shown in the top row of Fig. 8. Individual cells on either side of the boundary were tracked (green and yellow arrowheads) and their spectral profiles unmixed revealing the expected higher levels of eGFP expression in the cell tracked in the midbrain (bottom row) compared with a cell tracked in the hindbrain (middle row) reflected by the respective areas underneath the unmixed eGFP reference profiles. Within the neuroepithelium, cells undergo interkinetic migration that is characterized by cellular and nuclear movements between the basal and apical surfaces, with cell division occurring at the apical side. It would be interesting to determine whether the fluorescence contribution from the citrine-H2B fusion protein, which labels nucleosomes, could be quantified as a means to track cell cycle dynamics. Intensity from the marker would presumably fluctuate as nuclear chromatin replicates and subsequently condenses prior to chromosome segregation.

4.6 Imaging In Situ Hybridization with Three-Dimensional Resolution

Having established that the broad 2P power spectrum of ultrashort pulses is useful for integrating molecular, cellular, and morphogenetic information in live organisms over time,
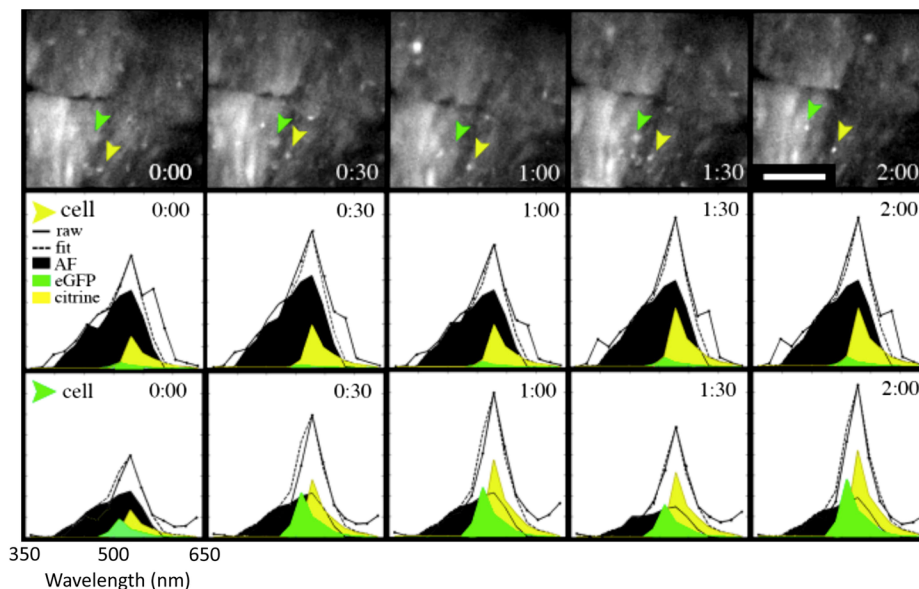
Fig. 8 Spectral unmixing of overlapping fluorescence spectra from live cells at the midbrain-hindbrain boundary. Stable transgenic embryos expressing eGFP in the *wnt1* lineage were injected at the one-cell stage with plasmid DNA containing a citrine-H2B fusion protein to mosaically mark inidividual nuclei. Top row shows summed spectral image, and arrowheads point to cells tracked in the midbrain (green arrowhead) and hindbrain (yellow arrohead). The spectral profiles of these cells were unmixed by varying weighting parameters for a linear sum of reference spectra (solid curves) to minimize the mean squared error between the proposed fit (dotted line) and measured data (solid line). Scale bar is 50 μm.
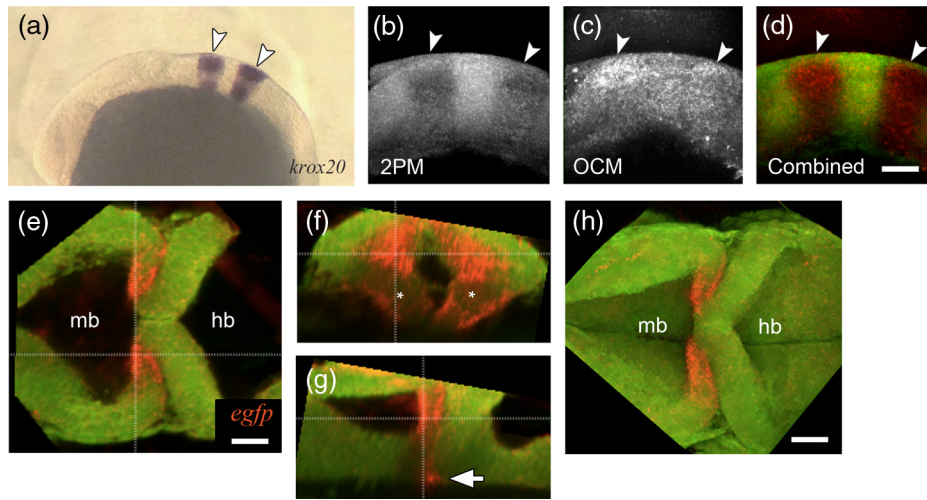
Fig. 9 Imaging gene expression domains with multimodal UPM. (a) Light microscopy image of an *in situ* hybridization (ISH), where the expression domain of the *krox20* gene is marked by NBT/BCIP staining (arrowheads). Combined 2PM-OCM from the embryo shows that NBT/BCIP quenches tissue autofluorescence (b), while it enhances scattering detected by OCM (c). When these signals are combined (d), the NBT/BCIP positive domains are marked by red, while the rest of the tissue is visible as either green (low OCM signal in tissue relative to autofluorescence) or yellow (comparable OCM signal in tissue relative to autofluorescence). (e–g) Optical sections of combined 2PM-OCM using ultrashort pulses from the midbrain–hindbrain boundary, showing where *egfp* transcripts are present in NBT/BCIP-stained embryos with 3-D resolution. Sections correspond to placement of cross-hairs. (e) En-face rendered image dependent on lateral resolution. Transcripts are localized to the MHB [(f) transverse and (g) lateral]. Optical sections depend on axial resolution. Asterisks point to characteristic lessening of staining intensity in the basal portion of the neural tube at the MHB. Arrow points to NBT/BCIP staining in the most ventral portion of the neural tube, at a depth of about 180 μm. (h) The 3-D maximum intensity projection of the same dataset as (e–g). Scale bars are 50 μm.

we sought to take advantage of the short coherence length of such pulses to provide complementary data on mRNA transcript localization. Though fluorescent staining can be employed for transcript detection and confocal or 2PM can be used to image transcript localization with 3-D resolution, such protocols are notoriously fickle to the degree that many developmental biologists continue to use the more classical chromogenic precipitate, NBT/BCIP. There have been reports of both confocal imaging based on backscattering[78] and a deep-red fluorescence emission[79] from NBT/BCIP for determining transcript localization in 3-D. While we were not able to detect NBT/BCIP excited fluorescence with our ultrashort pulses centered at 800 nm, we were able to detect backscattered light. Simultaneous imaging of tissue

autofluorescence, which is significantly quenched by NBT/BCIP, can be used to highlight domains of NBT/BCIP staining, as shown in Figs. 9(a)–9(d). Figure 9(a) shows NBT/BCIP staining marking the location of *krox20*, which is expressed in rhombomeres 3 and 5 of the developing hindbrain, in an easily distinguisable pattern. Figure 9(b) shows the quenching that occurs in that region. Figure 9(c) shows the OCM signal from both the tissue and NBT/BCIP stain. The overlay, shown in Fig. 9(d), highlights regions stained by NBT/BCIP (low autofluorescence and high OCM signal) in red, while tissue architecture (marked by comparable OCM and autofluorescence signal) is shown in green to yellow.

To demonstrate how this OCM technique can be used to complement 2PM data, we performed ISH to detect *egfp* transcripts in the stable transgenic line, where eGFP is driven by *wnt1* enhancer elements, and imaged those embryos with combined 2PM-OCM at 24 hpf [Figs. 9(e)–9(h)]. Comparing the distribution of *egfp* transcripts versus eGFP protein revealed that a substantial portion of the *wnt1* lineage stopped expressing the *wnt1* reporter, as suggested by tracking eGFP protein signal over time. Although this type of analysis can only be performed for a single time point in a given embryo, it will be useful for characterization of the genetic networks governing cell fate decisions during embryogenesis, as they involve not only the turning on of certain genes, but also the silencing of others.
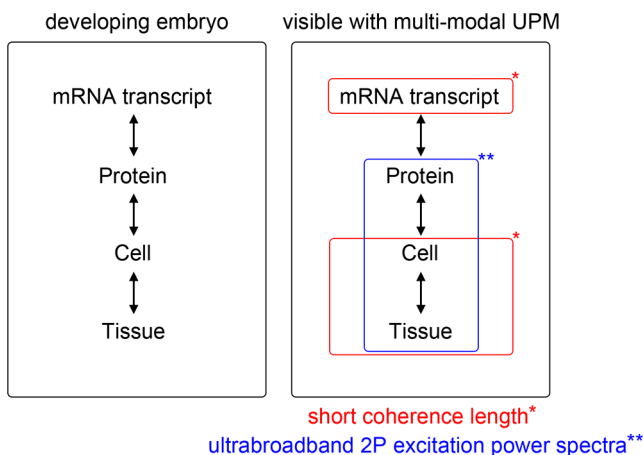
Fig. 10 Integrated imaging of multiscale embryonic development using multimodal UPM. Left diagram depicts the components that drive embryogenesis in a dynamic, responsive manner. Right diagram highlights the components that can be visualized simultaneously with multimodal UPM.

5 Conclusion

We have provided both theoretical arguments and data in favor of the use of ultrashort pulses for imaging the dynamic multiparameter mechanisms of embryonic development that begin at the molecular scale and culminate in the shaping of an entire organism. In particular, we have shown (1) the ability to image tissue morphogenesis and individual cells and

their movements within developing embryos from intrinsic autofluorescence, i.e., label free, (2) the ability to simultaneously track tissue morphogenesis and genetically labeled cell lineages, (3) the ability to excite a wide range of fluorescent protein markers simultaneously for tracking multiple genetically labeled lineages in their morphological context, and (4) the ability to image mRNA transcript localization marked by NBT/BCIP staining with 3-D resolution. These capabilities, summarized in Fig. 10, are available with a simple implementation for dispersion control, double-chirped mirrors which are relatively easy to align and produce less unwanted third-order dispersion (TOD) than prism pairs.[80]

In reality, it is highly unlikely we have achieved the theoretical enhancement predicted for transform-limited pulses. It will be interesting in the future to implement more sophisticated pulse-control methods for managing TOD such as MIIPs pulse shaping,[81] MEMs,[82] or a grating/prism compressor[83] that could be used to tune second- and third-order dispersions simultaneously. Such improvements may be used to more precisely account for varying imaging conditions and biological samples, further increase imaging speed, or if needed, decrease irradiation to the embryo while maintaining the same signal level.

Acknowledgments

References

1. H. Spemann and H. Mangold, "The induction of embryonic predispositions by implantation of organizers foreign to the species," *Arch. Mikr. Anat. Entwicklungsmechanik* **100**(3/4), 599–638 (1924).
2. M. C. Mullins et al., "Large-scale mutagenesis in the zebrafish—in search of genes-controlling development in a vertebrate," *Curr. Biol.* **4**(3), 189–202 (1994).
3. L. Solnica-Krezel, A. F. Schier, and W. Driever, "Efficient recovery of ENU-induced mutations from the zebrafish germline," *Genetics* **136**(4), 1401–1420 (1994).
4. J. Garciafernandez and P. W. H. Holland, "Archetypal organization of the amphioxus HOX gene-cluster," *Nature* **370**(6490), 563–566 (1994).
5. N. Soshnikova et al., "Duplications of HOX gene clusters and the emergence of vertebrates," *Dev. Biol.* **378**(2), 194–199 (2013).
6. O. Shimomura, F. H. Johnson, and Y. Saiga, "Extraction, purification and properties of aequorin, a bioluminescent protein from luminous hydromedusan, aequorea," *J. Cell. Comp. Physiol.* **59**(3), 223–239 (1962).
7. R. Heim, A. B. Cubitt, and R. Y. Tsien, "Improved green fluorescence," *Nature* **373**(6516), 663–664 (1995).
8. M. Chalfie et al., "Green fluorescent protein as a marker for gene-expression," *Science* **263**(5148), 802–805 (1994).
9. R. N. Bamford et al., "Loss-of-function mutations in the EGF-CFC gene CFC1 are associated with human left-right laterality defects," *Nat. Genet.* **26**(3), 365–369 (2000).
10. B. Ciruna et al., "Planar cell polarity signalling couples cell division and morphogenesis during neurulation," *Nature* **439**(7073), 220–224 (2006).
11. D. B. Sparrow et al., "A mechanism for gene-environment interaction in the etiology of congenital scoliosis," *Cell* **149**(2), 295–306 (2012).
12. M. J. Dixon et al., "Cleft lip and palate: understanding genetic and environmental influences," *Nat. Rev. Genet.* **12**(3), 167–178 (2011).
13. J. A. Marrs et al., "Zebrafish fetal alcohol syndrome model: effects of ethanol are rescued by retinoic acid supplement," *Alcohol* **44**(7–8), 707–715 (2010).
14. N. Yang et al., "Generation of oligodendroglial cells by direct lineage conversion," *Nat. Biotechnol.* **31**(5), 434–439 (2013).
15. A. Margariti et al., "Direct reprogramming of fibroblasts into endothelial cells capable of angiogenesis and reendothelialization in tissue-engineered vessels," *Proc. Natl. Acad. Sci. U. S. A.* **109**(34), 13793–13798 (2012).
16. T. Vierbuchen et al., "Direct conversion of fibroblasts to functional neurons by defined factors," *Nature* **463**(7284), 1035–1050 (2010).
17. C. B. Kimmel et al., "Stages of embryonic-development of the zebrafish," *Dev. Dynam.* **203**(3), 253–310 (1995).
18. K. Woo, J. Shih, and S. E. Fraser, "Fate maps of the zebrafish embryo," *Curr. Opin. Genet. Dev.* **5**(4), 439–443 (1995).
19. N. Olivier et al., "Cell lineage reconstruction of early zebrafish embryos using label-free nonlinear microscopy," *Science* **329**(5994), 967–971 (2010).
20. C. A. Ettensohn, "Encoding anatomy: developmental gene regulatory networks and morphogenesis," *Genesis* **51**(6), 383–409 (2013).
21. A. Streit et al., "Experimental approaches for gene regulatory network construction: the chick as a model system," *Genesis* **51**(5), 296–310 (2013).
22. P. J. Keller et al., "Reconstruction of zebrafish early embryonic development by scanned light sheet microscopy," *Science* **322**(5904), 1065–1069 (2008).
23. S. G. Megason and S. E. Fraser, "Imaging in systems biology," *Cell* **130**(5), 784–795 (2007).
24. W. Denk, J. H. Strickler, and W. W. Webb, "2-photon laser scanning fluorescence microscopy," *Science* **248**(4951), 73–76 (1990).
25. W. Supatto, "Advances in multiphoton microscopy for imaging embryos," *Curr. Opin. Genet. Dev.* **21**(5), 538–548 (2011).
26. J. Squier and M. Muller, "High resolution nonlinear microscopy: a review of sources and methods for achieving optimal imaging," *Rev. Sci. Instrum.* **72**(7), 2855–2867 (2001).
27. A. McMahon et al., "Dynamic analyses of drosophila gastrulation provide insights into collective cell migration," *Science* **322**(5907), 1546–1550 (2008).
28. F. Amat and P. J. Keller, "Towards comprehensive cell lineage reconstructions in complex organisms using light-sheet microscopy," *Dev. Growth Differ.* **55**(4), 563–578 (2013).
29. T. V. Truong et al., "Deep and fast live imaging with two-photon scanned light-sheet microscopy," *Nat. Methods* **8**(9), 757–102 (2011).
30. T. A. Planchon et al., "Rapid three-dimensional isotropic imaging of living cells using Bessel beam plane illumination," *Nat. Methods* **8**(5), 417–468 (2011).
31. D. Huang et al., "Optical coherence tomography," *Science* **254**(5035), 1178–1181 (1991).
32. S. Bhat et al., "4D reconstruction of the beating embryonic heart from two orthogonal sets of parallel optical coherence tomography slice-sequences," *IEEE Trans. Med. Imaging* **32**(3), 578–588 (2013).
33. I. V. Larina et al., "Sequential Turning Acquisition and Reconstruction (STAR) method for four-dimensional imaging of cyclically moving structures," *Biomed. Opt. Express* **3**(3), 650–660 (2012).
34. I. V. Larina et al., "Optical coherence tomography for live imaging of mammalian development," *Curr. Opin. Genet. Dev.* **21**(5), 579–584 (2011).
35. S. H. Syed et al., "Optical coherence tomography for high-resolution imaging of mouse development in utero," *J. Biomed. Opt.* **16**(4), 046004 (2011).
36. M. E. Akam, "The location of ultrabithorax transcripts in drosophila tissue sections," *EMBO J.* **2**(11), 2075–2084 (1983).
37. A. M. Larson and A. T. Yeh, "Ex vivo characterization of sub-10-fs pulses," *Opt. Lett.* **31**(11), 1681–1683 (2006).
38. K. Khairy and P. J. Keller, "Reconstructing embryonic development," *Genesis* **49**(7), 488–513 (2011).
39. C. C. Fowlkes et al., "A quantitative spatiotemporal atlas of gene expression in the Drosophila blastoderm," *Cell* **133**(2), 364–374 (2008).
40. Z. R. Bao et al., "Automated cell lineage tracing in Caenorhabditis elegans," *Proc. Natl. Acad. Sci. U. S. A.* **103**(8), 2707–2712 (2006).
41. C. J. Bardeen et al., "Effect of pulse shape on the efficiency of multiphoton processes: Implications for biological microscopy," *J. Biomed. Opt.* **4**(3), 362–367 (1999).
42. A. T. Yeh et al., "Advances in nonlinear optical microscopy for visualizing dynamic tissue properties in culture," *Tissue Eng. B-Rev.* **14**(1), 119–131 (2008).
43. D. Meshulach and Y. Silberberg, "Coherent quantum control of two-photon transitions by a femtosecond laser pulse," *Nature* **396**(6708), 239–242 (1998).
44. M. A. Albota, C. Xu, and W. W. Webb, "Two-photon fluorescence excitation cross sections of biomolecular probes from 690 to 960 nm," *Appl. Opt.* **37**(31), 7352–7356 (1998).
45. J. P. Ogilvie et al., "Fourier transform measurement of two-photon excitation spectra: applications to microscopy and optimal control," *Opt. Lett.* **30**(8), 911–913 (2005).
46. K. A. Walowicz et al., "Multiphoton intrapulse interference. 1. Control of multiphoton processes in condensed phases," *J. Phys. Chem. A* **106**(41), 9369–9373 (2002).
47. H. Hashimoto et al., "Measurement of two-photon excitation spectra of fluorescent proteins with nonlinear Fourier-transform spectroscopy," *Appl. Opt.* **49**(17), 3323–3329 (2010).
48. S. Pang et al., "Beyond the 1/T-p limit: two-photon-excited fluorescence using pulses as short as sub-10-fs," *J. Biomed. Opt.* **14**(5), 054041 (2009).
49. C. Wang and A. T. Yeh, "Two-photon excited fluorescence enhancement with broadband versus tunable femtosecond laser pulse excitation," *J. Biomed. Opt.* **17**(2), 025003 (2012).

50. W. Drexler et al., "In vivo ultrahigh-resolution optical coherence tomography," *Opt. Lett.* **24**(17), 1221–1223 (1999).
51. J. A. Izatt et al., "Optical coherence tomography and microscopy in gastrointestinal tissues," *IEEE J. Sel. Top. Quant. Electron.* **2**(4), 1017–1028 (1996).
52. J. M. Schmitt, "Optical coherence tomography (OCT): a review," *IEEE J. Sel. Top. Quant. Electron.* **5**(4), 1205–1215 (1999).
53. Q. F. Wu, B. E. Applegate, and A. T. Yeh, "Cornea microstructure and mechanical responses measured with nonlinear optical and optical coherence microscopy using sub-10-fs pulses," *Biomed. Opt. Express* **2**(5), 1135–1146 (2011).
54. A. M. Larson et al., "Ultrashort pulse multispectral non-linear optical microscopy," *J. Innov. Opt. Health Sci.* **2**(1), 27–35 (2009).
55. M. Westerfield, *The Zebrafish Book [A Guide for the Laboratory Use of Zebrafish (Danio rerio)]*, University of Oregon Press, Eugene, OR (2000).
56. G. R. Buckles et al., "Combinatorial Wnt control of zebrafish midbrain-hindbrain boundary formation," *Mech. Dev.* **121**(5), 437–447 (2004).
57. J. Schindelin et al., "Fiji: an open-source platform for biological-image analysis," *Nat. Methods* **9**(7), 676–682 (2012).
58. H. C. Peng et al., "V3D enables real-time 3D visualization and quantitative analysis of large-scale biological image data sets," *Nat. Biotechnol.* **28**(4), 348–375 (2010).
59. B. A. Filas et al., "A potential role for differential contractility in early brain development and evolution," *Biomech. Model. Mechanobiol.* **11**(8), 1251–1262 (2012).
60. V. D. Varner and L. A. Taber, "Not just inductive: a crucial mechanical role for the endoderm during heart tube assembly," *Development* **139**(9), 1680–1690 (2012).
61. J. A. Lister, "Development of pigment cells in the zebrafish embryo," *Microsc. Res. Tech.* **58**(6), 435–441 (2002).
62. M. Rhinn and M. Brand, "The midbrain-hindbrain boundary organizer," *Curr. Opin. Neurobiol.* **11**(1), 34–42 (2001).
63. W. Wurst and L. Bally-Cuif, "Neural plate patterning: upstream and downstream of the isthmic organizer," *Nat. Rev. Neurosci.* **2**(2), 99–108 (2001).
64. S. H. Huang, A. A. Heikal, and W. W. Webb, "Two-photon fluorescence spectroscopy and microscopy of NAD(P)H and flavoprotein," *Biophys. J.* **82**(5), 2811–2825 (2002).
65. E. R. Greenhill et al., "An iterative genetic and dynamical modelling approach identifies novel features of the gene regulatory network underlying melanocyte development," *Plos Genet.* **7**(9), e1002265(2011).
66. D. W. Raible et al., "Segregation and early dispersal of neural crest cells in the embryonic zebrafish," *Dev. Dynam.* **195**(1), 29–42 (1992).
67. K. L. Taylor et al., "Differentiated melanocyte cell division occurs in vivo and is promoted by mutations in Mitf," *Development* **138**(16), 3579–3589 (2011).
68. N. Russek-Blum et al., "Dopaminergic neuronal cluster size is determined during early forebrain patterning," *Development* **135**(20), 3401–3413 (2008).
69. Y. Dancik et al., "Use of multiphoton tomography and fluorescence lifetime imaging to investigate skin pigmentation in vivo," *J. Biomed. Opt.* **18**(2), 026022 (2013).
70. C. Antoniou et al., "Analysis of the melanin distribution in different ethnic groups by in vivo laser scanning microscopy," *Laser Phys. Lett.* **6**(5), 393–398 (2009).
71. A. P. McMahon and A. Bradley, "The WNT-1 (INT-1) protooncogene is required for development of a large region of the mouse-brain," *Cell* **62**(6), 1073–1085 (1990).
72. A. C. Lekven et al., "wnt1 and wnt10b function redundantly at the zebrafish midbrain-hindbrain boundary," *Dev. Biol.* **254**(2), 172–187 (2003).
73. L. A. Lowery and H. Sive, "Strategies of vertebrate neurulation and a re-evaluation of teleost neural tube formation," *Mech. Dev.* **121**(10), 1189–1197 (2004).
74. J. H. Gutzman et al., "Formation of the zebrafish midbrain-hindbrain boundary constriction requires laminin-dependent basal constriction," *Mech. Dev.* **125**(11–12), 974–983 (2008).
75. A. Kaufmann et al., "Multilayer mounting enables long-term imaging of zebrafish development in a light sheet microscope," *Development* **139**(17), 3242–3247 (2012).
76. I. Saytashev et al., "Pulse duration and energy dependence of photodamage and lethality induced by femtosecond near infrared laser pulses in Drosophila melanogaster," *J. Photochem. Photobiol. B-Biol.* **115**, 42–50 (2012).
77. M. Drobizhev et al., "Absolute two-photon absorption spectra and two-photon brightness of orange and red fluorescent proteins," *J. Phys. Chem. B* **113**(4), 855–859 (2009).
78. G. Jekely and D. Arendt, "Cellular resolution expression profiling using confocal detection of NBT/BCIP precipitate by reflection microscopy," *Biotechniques* **42**(6), 751–755 (2007).
79. L. A. Trinh et al., "Fluorescent in situ hybridization employing the conventional NBT/BCIP chromogenic stain," *Biotechniques* **42**(6), 756–759 (2007).
80. N. Matuschek, F. X. Kartner, and U. Keller, "Theory of double-chirped mirrors," *IEEE J. Sel. Top. Quant. Electron.* **4**(2), 197–208 (1998).
81. P. Xi et al., "Greater signal, increased depth, and less photobleaching in two-photon microscopy with 10 fs pulses," *Opt. Commun.* **281**(7), 1841–1849 (2008).
82. N. Olivier, D. Debarre, and E. Beaurepaire, "Dynamic aberration correction for multiharmonic microscopy," *Opt. Lett.* **34**(20), 3145–3147 (2009).
83. V. K. Chauhan et al., "Distortion-free single-prism/grating ultrashort laser pulse compressor," *IEEE J. Quant. Electron.* **46**(12), 1726–1731 (2010).

Holly C. Gibbs earned her BS in biomedical engineering from Texas A&M University in 2006 and MSc in genomics and pathways biology from the University of Edinburgh in 2008. Currently, she is a doctoral candidate in the Tissue Microscopy Lab in the Department of Biomedical Engineering at Texas A&M University where she specializes in the application of ultrashort laser technology in the field of developmental biology, specifically vertebrate brain patterning and development.

Yuquiang Bai earned his BS in physics from Shanxi University in 1999 and an MS in optics from the Shanghai Jiao Tong University in 2002. He worked in the telecommunications industry for four years and is currently a doctoral candidate in the Tissue Microscopy Lab in the Department of Biomedical Engineering at Texas A&M University where he specializes in optical coherence instrumentation and its application to imaging dynamic cell-matrix interactions and remodeling in engineered tissues.

Arne C. Lekven earned his BA in animal physiology from UCSD in 1989 and his PhD in Molecular, Cell, and Developmental Biology at UCLA in 1996. His postdoctoral training at the University of Washington School of Medicine centered on zebrafish development. He is an associate professor of biology at Texas A&M University and focuses on the role of Wnt signaling in patterning and growth during mesoderm induction and midbrain-hindbrain boundary formation.

Alvin T. Yeh earned his BSE in chemical engineering from the University of Michigan in 1993 and completed his PhD in chemistry at the University of California at Berkeley in 2000. Currently, he is associate professor of biomedical engineering at Texas A&M University, where his research focuses on instrumentation development for imaging modalities using ultrashort pulses and their application to study angiogenesis and cell–matrix interactions in engineered tissues and embryonic development.